Accepted manuscript

https://doi.org/10.1039/C9DT02768H

Dalton Trans., 2019,**48**, 13651-13661

ARTICLE

Unprecedented rock-salt ordering of A and B cations in the double perovskite $Nd_{2-x}Ca_xMgTiO_{6-\delta}$ and defect association

Received 00th January 20xx,
Accepted 00th January 20xx

DOI: 10.1039/x0xx00000x

M. Teresa Azcondo,[*a] Khalid Boulahya,[b] Clemens Ritter,[c] Flaviano García-Alvarado[a] and Ulises Amador[a]

The partial substitution of up to 5% Nd^{+3} by Ca^{+2} results in the oxide $Nd_{1.90}Ca_{0.10}MgTiO_{5.94}$ that presents some remarkable structural features with noticeable influence on its properties. In this oxide with monoclinic perovskite-like structure and octahedral tilting scheme ($a^-a^-b^+$), both A- and B-ions are arranged in a rock-salt like manner and represents thereby the first example of a type of perovskite theoretically predicted. Besides this unprecedented arrangement of A- and B-ions, the oxygen vacancies created through doping with acceptor ions are trapped by association with the acceptor defects ($V_O^{\bullet\bullet}$-$Ca_{Nd}^{'}$) and hence the mobility of these vacancies is strongly limited. The oxygen conductivity of the substituted material is lower and the activation energy for oxygen motion higher than those of the parent oxide, in which the concentration of anions vacancies is only due to intrinsic defects.

Introduction

Solid oxide fuel cells (SOFCs) are at the focus of a growing research activity to make them an effective alternative to the highly polluting energy-conversion devices based on fossil fuels. Many materials have been synthetized and studied to determine their suitability as anode or cathode for SOFCs.[1] Among them, some mixed oxides with perovskite structure are outstanding components of both types of electrodes. For its part, the electrolyte plays a key role in operating SOFCs allowing the diffusion of the large O^{-2} ions through its structure. This is an unusual physicochemical property as reveals the scarce number of pure oxide-ion conductive materials. Some mixed oxides with perovskite structure,[2] as $LaGaO_3$ based compounds,[3] stand out from the rest thanks to their high ionic conductivity at intermediate temperatures (923 < T < 1073 K). The perovskite structure is able to accommodate a large variety of elements and cation oxidation states.[4] Aliovalent substitution may be accompanied by either changes in oxidation state or by the creation of extended oxide ion defects or even both in different extent. These two compensating mechanisms can be found in the same family of compounds depending on the particular composition and crystal chemistry of the transition metals. This is, for example, the case of the compounds derived from the titanates La_2MTiO_6, with M= Ni or Co for which the compensating mechanism is different upon partial substitution of lanthanum by strontium,[5, 6] or by creation of lanthanum vacancies.[7, 8] Following a preliminary evaluation, some of these materials are found to display noticeable properties as cathode components in SOFCs. In particular the y = 0.14 member of the $La_{2-y}NiTiO_{6-\delta}$ series[8] and the y = 0.05 member of the $La_{2-y}CoTiO_{6-\delta}$ series[7] exhibit promising performances since their polarization resistances (0.50 Ωcm² and 0.39 Ωcm² at 1073 K, respectively) are better than the state-of-the-art $La_{1-x}Sr_xMnO_3$-based cathodes.[9] The study of the above-mentioned titanates was carried out using common electrolytes (yttria-stabilized zirconia (YSZ) or gadolinia-doped ceria (CGO)) showing good chemical and mechanical compatibility under cathodic conditions. However, it would be desirable to use a more suitable solid electrolyte from the chemical and mechanical points of view. Chemical compatibility and minimal mismatch in the thermal expansion coefficients, both in reducing and oxidizing atmospheres at the working temperature of SOFCs will ensure adequate durability. These two goals could be achieved using as electrolyte a titanate with composition and structure similar to those of the electrode materials. Thus, we have studied the effect of Ca-doping at the Nd-site in the stoichiometric host Nd_2MgTiO_6, which shows a double perovskite structure.[10] Such substitution is intended to produce oxygen vacancies as charge compensation mechanism because no oxidation of any other cation in the structure

[a] *Universidad San Pablo-CEU, CEU Universities, Facultad de Farmacia, Departamento de Química y Bioquímica, Urbanización Montepríncipe, Boadilla del Monte, E-28668, Madrid, Spain.*

[b] *Departamento de Química Inorgánica, Facultad de Química, Universidad Complutense, E-28040 Madrid, Spain.*

[c] *Institut Laue-Langevin, BP 156-38042 Grenoble Cedex 9, France.*

‡Electronic Supplementary Information (ESI) available: Fig. SI 1. XRD patterns of $Nd_{2-x}Ca_xMgTiO_{6-\delta}$ (x= 0, 0.10, 0.20 and 0.30); Fig. SI 2. BSE image of a $Nd_{1.8}0Ca_{0.20}MgTiO_{6-\delta}$ sample; Fig. SI 3. Magnetic susceptibility data for $Nd_{2-x}Ca_xMgTiO_{6-\delta}$ (x= 0, 0.10); Fig. SI 4. Low-angle zone of the NPD data for x=0.10 fitted to two structural models; Table SI 1. Nominal and experimental (EDS) compositions for the $Nd_2MgTiO_{6-\delta}$ sample; Table SI 2. Nominal and experimental (EDS) compositions for the $Nd_{1.9}0Ca_{0.10}MgTiO_{6-\delta}$ sample; Table SI 3. Refined structural parameters for $Nd_{2-x}Ca_xMgTiO_{6-\delta}$ (x= 0, 0.10); Table SI 4. Selected structural information for $Nd_{2-x}Ca_xMgTiO_{6-\delta}$ (x=0, 0.10); Table SI 5. Curie constant C and Weiss temperature θ for $Nd_{2-x}Ca_xMgTiO_{6-\delta}$ (x= 0, 0.10). See DOI: 10.1039/x0xx00000x

seems feasible. Thus, we have prepared the series $Nd_{2-x}Ca_xMgTiO_{6-\delta}$ ($0 \le x \le 0.30$) and investigated its electrical conductivity. Interestingly, the vacancies created upon doping have very low mobility owing to defect association. Even more, ionic conduction is higher in the parent compound, x = 0. A combination of structural and microstructural techniques has unveiled the origin of the observed behaviour. Furthermore, an unprecedented rock-salt ordering in A- and B-position of perovskite structure has been found and related to defect association.

Experimental

Sample preparation and composition determination

The series of samples $Nd_{2-x}Ca_xMgTiO_{6-\delta}$ with x = 0, 0.10, 0.20 and 0.30 have been synthesized by a modified Pechini method. They were prepared by dissolving stoichiometric amounts of high-purity $Nd(NO_3)_3 \bullet 6H_2O$ (99.9%), $Mg(NO_3)_2 \bullet 6H_2O$ (99.0%) and $CaCO_3$ (99.9%) in acidified water (using HNO_3); insoluble TiO_2 (anatase 99.9%) was added to form an homogeneous suspension. After polymerization induced by ethylenglycol, the obtained resin was calcined to remove the organic matter at 900ºC for 12 hours, a final treatment at 1673 K for 24 hours was applied to obtain well crystallized single phase samples. Along the synthesis several intermediate grindings were applied. All reactants were from Aldrich and prior to be used their actual contents of metals were determined by thermogravimetric analysis (TGA).

The samples´ purity was checked by powder X-ray diffraction (XRD), using the apparatus described below.

The chemical composition of the samples was semi-quantitatively determined on sintered pellets by electron dispersive spectroscopy (EDS) on a FEI XL30 scanning microscope using an EDAX detector; about 20 crystals of every sample were probed.

Structural and microstructural characterization

High-resolution X-ray diffraction (XRD) patterns were collected on a Bruker D8 high-resolution diffractometer, working with a monochromatic Cu(Kα1) (λ=1.5406 Å) radiation obtained using a germanium monochromator, and equipped with LynxEye® rapid detector. Patterns were recorded in the angular range 20-140 (2θ(deg.)) with a step width 0.0197(2θ(deg.)) over a total exposure time period of 24 h. Some more relevant zones of the patterns were measured with better angular resolution (step width 0.0128 (2θ(deg.)) and higher counting statistics.

Neutron powder diffraction (NPD) patterns were recorded at room temperature on the high-resolution diffractometer D2B; a monochromatic beam of wavelength 1.594 Å was selected with a Ge monochromator from the primary beam. The instrumental resolution was increased by reducing the divergence of the primary beam by an additional 10' collimator. The instrumental contribution to the line broadening was determined using a NIST standard sample of $Na_2Ca_3Al_2F_{14}$; whereas a standard sample of Si (also from NIST) was used for the precise evaluation of the wavelength. The structural refinements were performed by the Rietveld method using the FullProf software.[11] The neutron scattering amplitudes used in the refinement were: 0.7690, 0.4700, -0.3438, 0.5375 and 0.5803 (10^{-12} cm) for Nd^{+3}, Ca^{+2}, Ti^{+4}, Mg^{+2} and O^{-2}, respectively; isotropic thermal factors (ITF) were used for all atoms. Throughout the refinements the perovskite B-sites were constrained to be fully occupied and a single thermal factor for all oxygen atoms was assumed.

The samples were furthermore characterized by electron diffraction and high resolution electron microscopy (HREM) using a Jeol 3000 FEG electron microscope, fitted with a double tilting goniometer stage (±20°, ±20°).

Electrical conductivity

Total electrical conductivity was determined by impedance spectroscopy (IS) under air, argon and pure oxygen in the temperature range 1073–773 K every 50 K after stabilization at each temperature for 1 hour. Densified pellets were used as probes, (ca. 8 mm diameter and ca. 1 mm thickness), with relative densifications around 85% referred to the crystallographic density; it was not possible to reach higher densification. The densest pellets were prepared by isostatic pressing the corresponding powders at 100 MPa sintered at 1773 K for 6 h and slowly cooled down to (2 K min^{-1}). Platinum electrodes were attached to pellet sides painted with a Pt paste (Fuel Cell Materials) and fired at 1173 K for 1 h. A Solartron 1260 FRA was employed with 100 mV AC perturbation in the 10^6–10^{-3} Hz frequency range; to fit the IS spectra to equivalent circuits the ZView software was used.[12]

Magnetic characterization

The temperature dependence of the molar dc magnetic susceptibility (χ) was measured using a superconducting quantum interference device magnetometer (Quantum Design, model MPMS-XL). Polycrystalline samples were measured according to the procedure described elsewhere.[13]

Results and discussion

Samples purity and chemical composition

Samples of the $Nd_{2-x}Ca_xMgTiO_{6-\delta}$ series (x= 0.0, 0.10, 0.20 and 0.30) prepared in air seem to be single-phase from routine XRD data. Profile fitting of room temperature data suggests a perovskite-like structure of monoclinic symmetry with a unit cell of dimensions $2^{1/2}a_p$ x $2^{1/2}a_p$ x $2a_p$ (where a_p refers to the unit cell of a cubic perovskite) and monoclinic angle, β, close to 90º. Fig. SI1 shows the corresponding graphic results for the four samples. This symmetry agrees with the tolerance factors (t) calculated for these perovskites, ranging from t = 0.9154 to t = 0.9190 for x = 0.00 and 0.30, respectively. The oxide Nd_2MgTiO_6 has previously been reported to adopt this monoclinic distortion of the perovskite structure, in agreement with the present results.[10] Similar unit cells have been used to describe many other perovskite-like compounds: Sr_2YNbO_6 [14] (t = 0.925) and Sr_2YbNbO_6 [15] (t = 0.932), $Sr_{2-y}LuNb_{1-x}Ti_xO_6$ ($0 \le x \le 0.2$).[16]

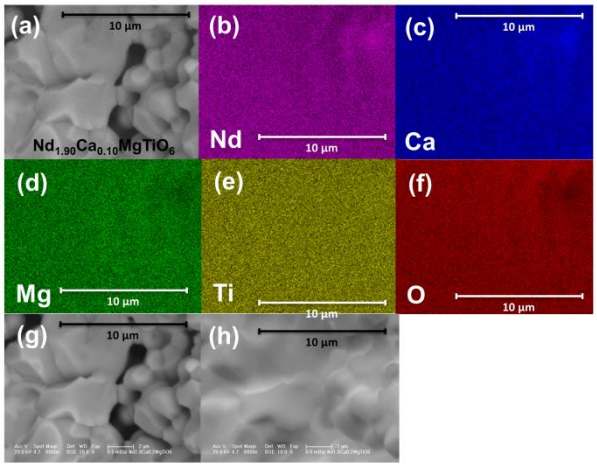

Figure 1. (a) Back-scattered electrons (BSE) image taken at a magnification of x 8000 and element-distribution maps of a $Nd_{1.90}Ca_{0.10}MgTiO_6$ sample: (b) Nd, (c) Ca, (d) Mg, (e) Ti and (f) O, respectively. (g) and (h) are BSE and the corresponding topographic images, respectively, showing the surface morphology responsible for some contrast effects in the element-maps.

Although XRD suggests that the solid solution $Nd_{2-x}Ca_xMgTiO_6$ extends up to x = 0.30, EDS analyses and SEM images clearly reveals that for samples with x ≥ 0.2 segregation occurs. Fig. SI1 demonstrates that the samples of nominal composition $Nd_{1.80}Ca_{0.20}MgTiO_6$ are not homogeneous. Phase separation occurs in all the batches with nominal composition x ≥ 0.2. On the contrary, the samples with 0 ≤ x ≤ 0.10 show no compositional inhomogeneity as evidenced in Fig. 1. EDS confirmed all of them to be single-phase; the actual chemical compositions being close to the nominal one within the experimental error (see Tables SI1 and SI2). More importantly, the distribution of all the elements is confirmed to be homogeneous throughout the samples. Fig. 1 shows the back-scattered electron (BSE) images of a sample $Nd_{1.90}Ca_{0.10}MgTiO_{6-\delta}$ (x=0.10), together with the corresponding element-distribution maps. The contrast in BSE images is sensitive to the average composition (light elements give dark contrasts, and vice-versa); thus Fig. 1a and 1g allow discarding any phase segregation. Element-distribution maps shown in Fig. 1b to 1f confirm the homogeneous composition of the sample. Darker and brighter zones observed in some of those images are artefacts due to the surface morphology (see Fig. 1h). Therefore, the limit of the aliovalent substitution of Nd^{+3} by Ca^{+2} in the title compounds is rather low, ($0.10 \leq x_{max} < 0.20$). We have studied the x = 0.00 and 0.10 materials more deeply by HREM and NPD prior to the electrical characterization.

Crystal structures

Monoclinic distortion of the cubic perovskite results because of the mismatch between the A-O and B-O distances, inducing a correlated tilting of the BO_6 octahedra. Thus, displacement of oxygen ions is the main structural effect related to the lowering in symmetry. In spite of the low X-ray scattering power of oxygen, it is possible to obtain conclusive evidences of the monoclinic distortion by a detailed analysis of some representative Bragg peaks in the powder XRD pattern.[16] In the diffraction patterns, the distortion is evidenced by the appearance of several sets of extra peaks in addition to the fundamental reflections of a typical simple cubic perovskite. Those fundamental reflections are clearly split at high diffraction angles, indicating a deviation from the cubic symmetry. For instance, the splitting of the $(222)_p$ simple-cubic-perovskite reflection into three, (see inset in Fig. 2a and 2b), suggests a triclinic distortion of the aristotype cubic cell. This triclinic cell can be converted into a primitive monoclinic one with lattice parameters $2^{1/2}a_p$ x $2^{1/2}a_p$ x $2a_p$ and β≈90º, which allows indexing all the observed peaks, as previously stated. Therefore, both the undoped $Nd_2MgTiO_{6-\delta}$ oxide as well as the Ca-containing one, $Nd_{1.90}Ca_{0.10}MgTiO_{6-\delta}$, display monoclinic symmetry. However, the group-subgroup relations in perovskites considering not only rigid tilting of octahedra but also different kinds of metal ordering either on A-sites or on B-sites has been well established by theory.[17-23] Thus, in the case of the un-doped compound S.G. (#14) $P2_1/n$ seems to be the most likely. This is very common in monoclinic perovskites with rock-salt cationic ordering on the B-sites,[19, 22, 23] resulting from the tilting of the BO_6 octahedra according to a scheme ($a^-a^-b^+$);[17] the octahedra tilting being a mechanism to accommodate the mismatch between the A-O and B-O distances.[4] For the Ca-doped perovskite the appearance of the (010) reflection (forbidden in S.G. $P2_1/n$) suggests a further lowering of symmetry. Even more, since this peak is clearly observed in the XRD pattern, (Fig. 2b), the structural effect responsible of the lower symmetry should be related to metal ions.

To obtain a detailed structural model, describing the partial substitution of Nd by Ca, the scheme of octahedral tilting, the ordering of B and/or A ions and the presence of oxygen vacancies, a series of HREM, EDS and NPD studies were performed on both samples $Nd_{2-x}Ca_xMgTiO_{6-\delta}$ (x=0.00 and 0.10). Many crystals (about three dozens) of each sample were analysed on the transmission electron microscope; in all cases, the composition was consistent with the nominal ones within the experimental error. This confirms the homogeneous distribution of elements, not only at microscopic level as suggested by SEM images (Fig. 1) but also at the atomic scale.

Concerning the structure models HREM gives crucial information. The un-doped oxide, Nd_2MgTiO_6, was studied along the most significant zone axes. In Fig. 3, the HREM micrograph along [010] shows an apparently well-ordered material with d-spacings of 7.6 Å and 5.4 Å, corresponding to d_{001} and d_{100}. Fast Fourier transformation (FFT) of the HREM micrograph was performed to detect the possible existence of different domains that could evidence the presence of an additional ordering of the structure. However, the whole crystal appears to be homogeneous with only maxima corresponding to the diagonal double perovskite unit cell being observed (Fig. 3a).

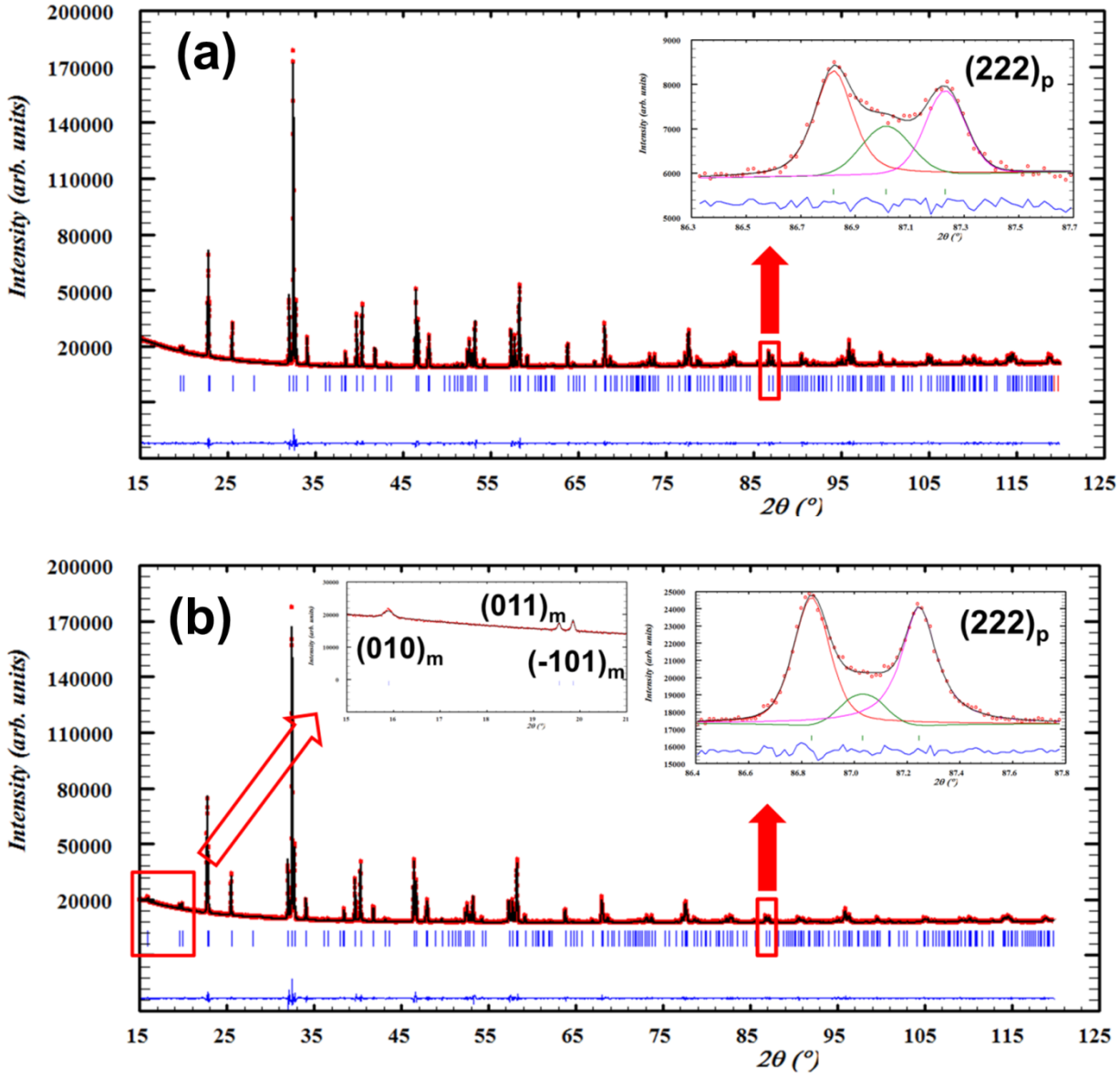

Figure 2. Experimental (red points), calculated (solid black line) and their difference (blue line at bottom) XRD patterns for Nd_2MgTiO_6 (a) and $Nd_{1.90}Ca_{0.10}MgTO_{6-\delta}$ (b). The vertical bars indicate the positions of the Bragg peaks. In the insets splitting of $(222)_p$ peak is depicted suggesting a monoclinic unit cell.

The contrast observed in this image consists of bright dots alternating with brightest ones, which can be associated with Mg atoms alternating with Ti ones along [100] and [001]. This contrast variation confirms that this material presents cationic ordering, which is also supported by NPD (see below).

The diffraction maxima observed in the FFT in Fig. 3a correspond to the reflection conditions h0l: h+l = 2n; h00: h = 2n and 00l: l = 2n which are compatible with S.G. $P2_1/n$.

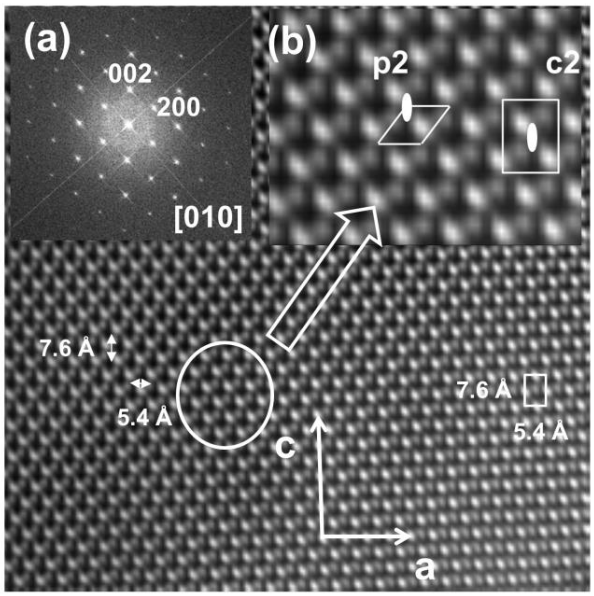

Figure 3. HREM image of Nd_2MgTiO_6 along [010]. (a) Optical FFT, (b) symmetry of the projected structure.

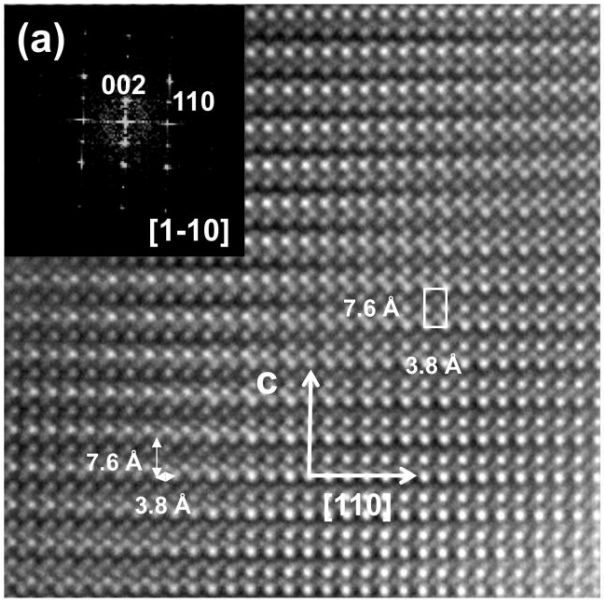

Figure 4. HREM image of $Nd_{1.90}Ca_{0.10}MgTiO_6$ along [1-10]. (a) Optical FFT.

The symmetry of the projected structure provides conclusive information about the 3D symmetry and hence helps to determine the actual space group. Fig. 3b displays an enlarged view of the HREM micrograph revealing the structure symmetry along [010]. In this figure the sole symmetry elements observed are two-fold axes perpendicular to the image plane, corresponding to the 2D groups p2 or c2 depending on the choice of the unit cell (in fact both plane groups are the same). This result confirms the S.G. proposed since this is the sole among the possible ones whose projection along [010] presents such planar symmetry.

The XRD pattern of the calcium-substituted material suggests that it presents a lower symmetry (Fig. 2b). To confirm this unexpected finding, HREM images were taken along some relevant directions. Fig. 4 displays the HREM image of the Ca-containing oxide along [1-10] suggesting a well ordered material confirmed by the corresponding FFT (Fig. 4a) which can be indexed with the above mentioned diagonal unit cell. The observed reflection conditions are consistent with those expected for S.G. $P2_1/n$.

Fig. 5 shows the HREM image taken along [001] and the corresponding FFT pattern. The latter confirms that the material is well-ordered and does not present any short-range effect. The diffraction pattern (Fig. 5a) clearly reveals the presence of (0k0) (k = 2n + 1) maxima which evidences a loss of symmetry from $P2_1/n$ to Pn, as already suggested by the XRD pattern shown in Fig. 2b.

The structure projected along this direction (Fig. 5b) presents pm plane symmetry, as expected for the S.G. Pn, confirming the lowering in symmetry induced by partial replacement of Nd by Ca.

Finally, in Fig. 6 the HREM along [100] is depicted. This image and the corresponding FFT confirm all the above-mentioned structural features: the material is well ordered, and the symmetry of the structure corresponds to S.G. Pn (#7) since its projection along [100] displays plane symmetry pg (Fig. 6b) as expected for this Space Group.

The structure of the parent oxide (Table SI3) shows a well-known monoclinic distortion of the cubic perovskite caused by the tilting of rigid BO_6 octahedra according to the scheme ($a^-a^-a^+$),[4, 17] which is very common in either orthorhombic (S.G. Pnma) or monoclinic (S.G: $P2_1/n$, as in the present case) perovskites.[5, 24] Fig. 7a shows the NPD patterns: experimental, calculated and their difference. Table SI4 gives selected structural information.

The origin of the monoclinic symmetry observed in this case is the ordering of Mg and Ti on the B site. While in an orthorhombic structure with the same tilting scheme there is only one crystallographic site for B cations, in the monoclinic model two independent crystallographic sites, 2d (½ 0 0) and 2c (½ 0 ½) for B´ and B´´ ions allow an ordered arrangement of the B-cations (Fig. 8a). Since the neutron scattering amplitudes of Ti and Mg are significantly different, the site occupancies can be readily determined. Refinements show that no antisite defects exist in this material since the ions sizes are significantly different ($^{VI}r(Mg^{+2})$= 0.72 Å) and $^{VI}r(Ti^{+4})$= 0.605 Å) as well as the cation charges.[25] Thus the Mg^{+2} cations occupy the B'-sites and the smaller Ti^{+4} ions occupy the B''-positions. It is well established that B-site cation ordering is promoted when the ionic size and/or charge difference of the B-ions are large[4] like in the present case. Bond valence sums (BVS) also confirm the cation ordering in the perovskite B-sites in this material. This result disagrees with the model reported in ref. [10] which considers ca 4% of AS defects.

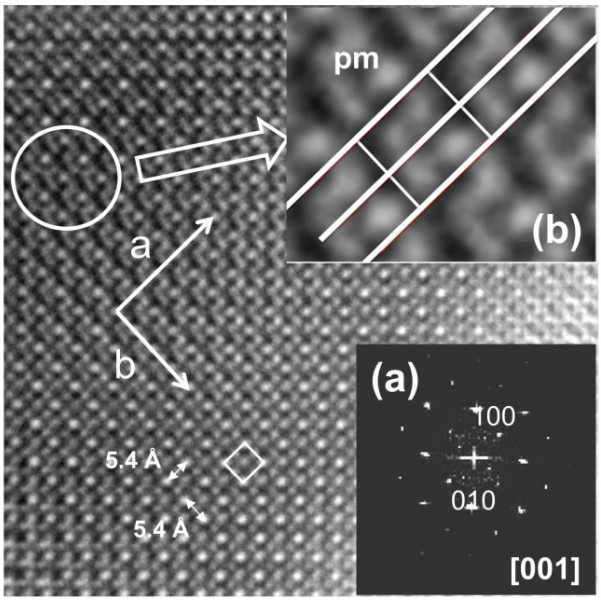

Figure 5. HREM image of $Nd_{1.90}Ca_{0.10}MgTiO_6$ along [001]. (a) Optical FFT. (b) symmetry of the projected structure.

Worth to note, other structural models involving A-site vacancies are ruled out based on magnetic measurements. Thus, magnetic susceptibility (χ) data obtained for x = 0.00 and x = 0.10 compounds confirmed the respective nominal amounts of the only paramagnetic cation present in both compounds, i.e., the Nd^{+3} ($4f^3$ configuration). In both oxides χ increases as temperature decreases from room temperature down to 2 K (see χ vs. T plot in Fig. SI 3) and in accordance with the Nd^{+3} contents the χ values obtained for x = 0.00 are slightly higher than those for x = 0.10. This is evident in the χ^{-1} vs T plot (Fig. SI 3). Furthermore, this plot shows the characteristic paramagnetic behaviour of Nd^{+3} cation under the influence of the crystal field created by the surrounding lattice.[26]

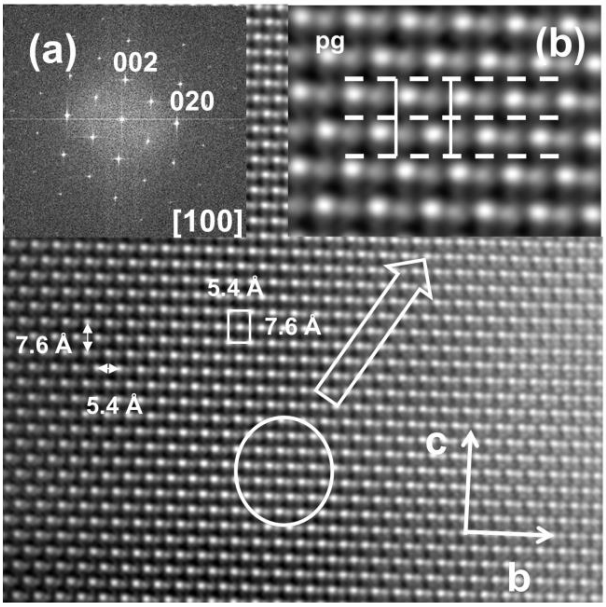

Figure 6. HREM image of $Nd_{1.90}Ca_{0.10}MgTiO_6$ along [100]. (a) Optical FFT. (b) symmetry of the projected structure.

Thus, linear dependence is observed from room temperature down to ~120 K and below this temperature χ^{-1} deviates downwards due to the crystal-field splitting of the ground J-multiplet $^4I_{9/2}$ of the Nd^{+3} cation. The magnetic susceptibility data above 150 K were fitted to the Curie-Weiss law $\chi = C/(T-\theta)$ and the best-fit values of the fitting parameters, namely the Curie constant C and the Weiss temperature θ, are shown in Table SI 5. The experimental magnetic moments determined for x = 0.00 and x = 0.10 compounds, 3.68±0.04 μ_B/Nd and 3.65±0.03 μ_B/Nd respectively, are in agreement with the theoretical magnetic moment for Nd^{+3} cation, 3.62 μ_B.[27]

As XRD pattern revealed and HREM images confirmed the partial substitution of Nd^{+3} by Ca^{+2} induces a lowering of symmetry from $P2_1/n$ to Pn. In the NPD pattern of the Ca-containing oxide the (010) peak (first Bragg peak at lowest angles in Fig. 7b) is clearly observed.

The fitting of the NPD data (Fig. 7b) confirms the metallic compositions to be the nominal one within experimental error. The final refined structural model suggests that the x = 0.10 perovskite presents some degree of anion vacancies created as charge compensating mechanism for the aliovalent replacement of Nd^{+3} by Ca^{+2}; accordingly to Kröger-Vink notation the mechanism can be described as in Eq(1):

$$2Nd_{Nd}^{x} + 2CaO + O_O^x \rightarrow 2Ca'_{Nd} + V_O^{\bullet\bullet} + Nd_2O_3 \quad (1)$$

As in the parent perovskite, Ti and Mg are ordered in a rock-salt like manner; however, on the contrary to what has been observed in that oxide, $Nd_{1.90}Ca_{0.10}MgTiO_{6-\delta}$ shows up to 14% of anti-site (AS) defects as Mg and Ti partially share B´ and B´´ sites (Table SI 3). The distribution of Ti^{+4} and Mg^{+2} as well as the presence of AS defects are confirmed by the B´-O and B´´-O distances as well as by the BVS shown in Table SI 4. Due to the lower symmetry, the BO_6 octahedra are more distorted in the Ca-containing perovskite than in the parent material (Table SI 4).

In the S.G. Pn the A-site in S.G. $P2_1/n$ splits into two, allowing ordering of Nd and Ca (Table SI 3). This structural effect suggested by the presence of the (010) peak in the XRD pattern (Fig. 2b) is confirmed by NPD. The order developed on the A-sites consists of a rock-salt arrangement of positions fully occupied by Nd^{+3} ions and positions shared by Nd^{+3} and Ca^{+2} cations. Thus, in this perovskite both A- and B-ions display rock-salt order (Fig. 8b). There are many perovskites with B-ions ordered in such a way, on the contrary, to our best knowledge; the present compound is an unprecedented example of a perovskite with rock-salt order of A-ions.

At this point it is worth to note that Ti^{+4} is prone to present second order Jahn-Teller (SJT) effect, which in these cases will result in its displacement from the centre of the TiO_6 octahedra, like in $BaTiO_3$.[28, 29]

ARTICLE

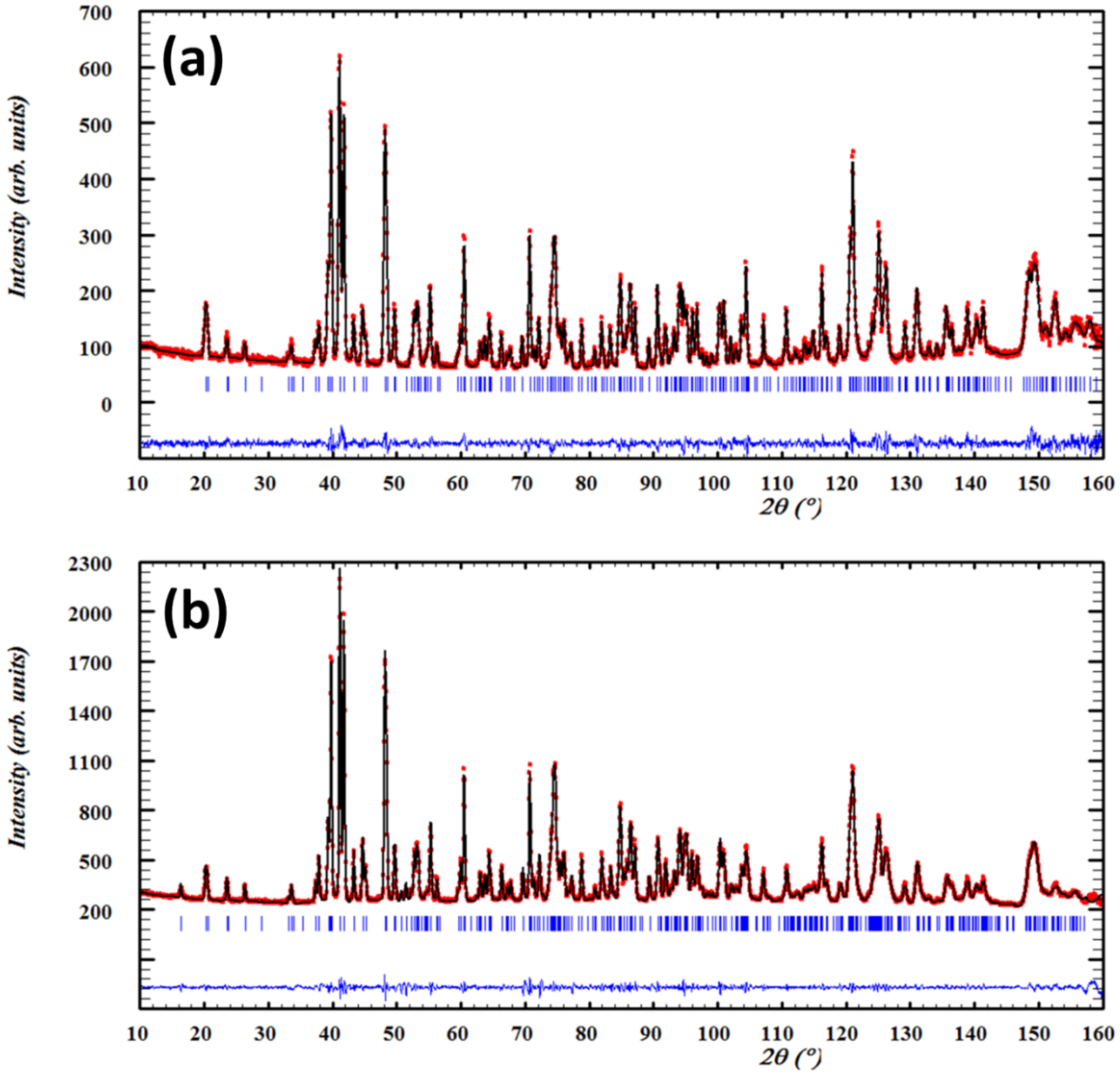

Figure 7. Experimental (red points), calculated (solid black line) and their difference (blue line at bottom) NPD patterns for Nd_2MgTiO_6 (a) and $Nd_{1.90}Ca_{0.10}MgTO_{6-\delta}$ (b). The vertical bars indicate the positions of the Bragg peaks.

This SJT effect would break the symmetry from $P2_1/n$ to Pn in both the pristine and the Ca-doped perovskite. However, this is not what we observe; only the Ca-containing oxide is non-centrosymmetric. As starting model we used a double perovskite-like structure with $P2_1/n$ symmetry; then the 2_1-axis is removed (Pn S.G.) and Ti-ions are allowed to move off the centre of the octahedral. Although the (0k0) k = 2n+1 maxima appear (Fig. SI 4), the SJT associated to Ti^{+4} only accounts for a fraction of the intensity of this family of peaks. This suggests that other structural feature is responsible for the loss of symmetry. Thus, the ordering of Ca^{+2} and Nd^{+3} is in the origin of the lowering of symmetry observed in the Ca-doped perovskite. Mg^{+2} and Ti^{+4} ions order since present a noticeably difference in charge and size; this is not the case for Ca^{+2} and Nd^{+3}.[25]

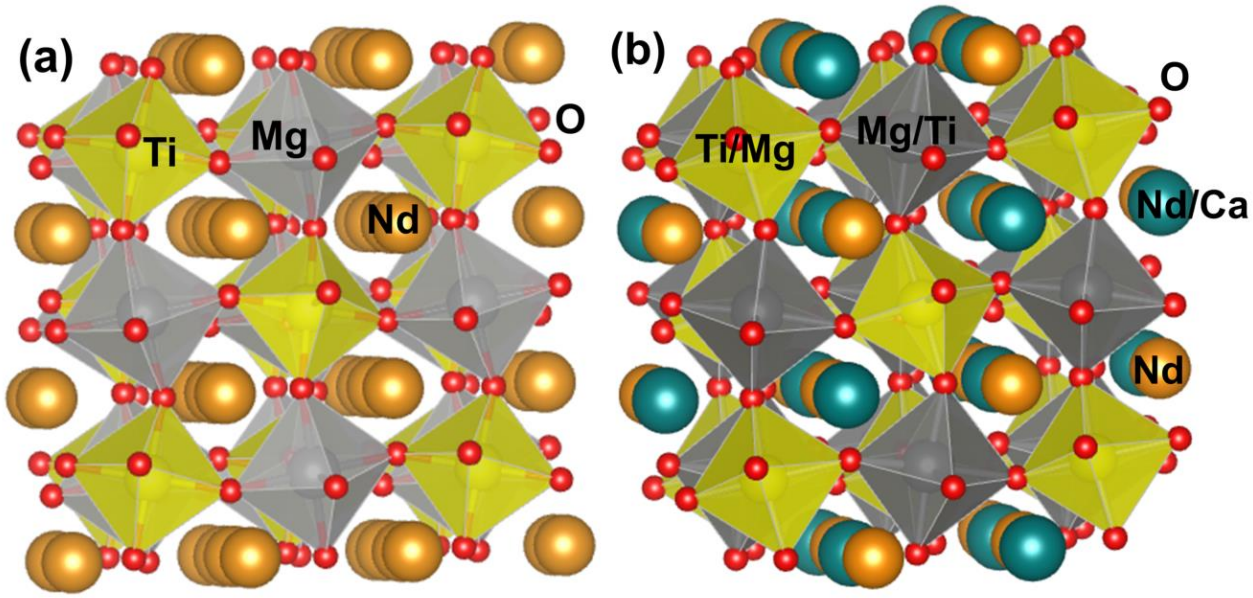

Figure 8. Schematic representation of the structure of parent Nd_2MgTiO_6 (a) and $Nd_{1.90}Ca_{0.10}MgTiO_{6-\delta}$ (b). In the former only B-ions present rock-salt order, whereas in the later both B- and A-ions are arranged in a rock-salt manner.

It is not evident the driven force to order these two ions, but it seems that the defect association depicted in Fig. 9b, ($V_O^{\bullet\bullet}$-$Ca_{Nd}^{'}$) revealed by the structural refinement (Tables SI 3 and SI 4), may play a role in the adoption of the rock-salt like ordering of A-ions.

The refinement of the NPD data reveals that oxygen vacancies are located only on O1a sites (Table SI 3) defining rows along the a-axis (Fig. 9a). This geometry could offer an easy path for oxide-ion diffusion and could therefore improve the ion conductivity in comparison with the parent perovskite. However, no increase of conductivity is observed (see next section). Inducing oxygen vacancies with acceptor dopants can in fact result in the trapping of these oxygen vacancies ($V_O^{\bullet\bullet}$) through the attractive electrostatic interactions between the positively charged anion vacancies and the negatively charged aliovalent cations ($Ca_{Nd}^{'}$). This effect would limit the ionic conductivity since the mobility of the oxygen vacancies is hindered. Fig. 9b shows that the O1a site (where oxygen vacancies are located) is coordinated to two Nd/Ca sites at distances much shorter than those to Nd ions (Fig. 9b).

Finally, as for the parent perovskite, structural models involving A-ions vacancies are discarded based on magnetic measurements.

Electrical properties

Representative impedance spectra are presented in Fig. 10 for both the parent and Ca-containing material recorded at 1073 K under argon atmosphere. These spectra consist of two arcs in the high- and middle-frequency range and one diffusion arc at low frequencies. The proposed equivalent circuit is depicted in the inset of Fig. 10 and can be schematized as: $(R_bQ_b)(R_{gb}Q_{gb})W_s$ which accounts for the bulk resistance and capacity in series with similar components for the grain boundaries and a diffusion element (Warburg impedance). The values of capacitances assigned to the bulk and grain-boundary processes are in the ranges: 8 10^{-13} to 2 10^{-12} F for the former and 8 10^{-10} to 9 10^{-12} F for the latter. These values confirm the assignment proposed[30]. Using this circuital model to fit the IS spectra of both samples, at different temperatures in different atmospheres, allows to obtain the bulk conductivities shown in Fig. 11 as an Arrhenius plot.

The total conductivity of both samples is independent of the oxygen partial pressure (pO_2) which can be taken as signature of its ionic character. Ionic conduction is also evidenced by the Warburg element in the equivalent circuit suited to fit the IS data. In any case, oxide conduction is low in both perovskites (1.40 10^{-5} and 6.14 10^{-6} Scm^{-1} for the parent and Ca-containing at 1073 K, respectively).

The Warburg impedance, which is always attributed to transport due to diffusion, is described by Eq(2):

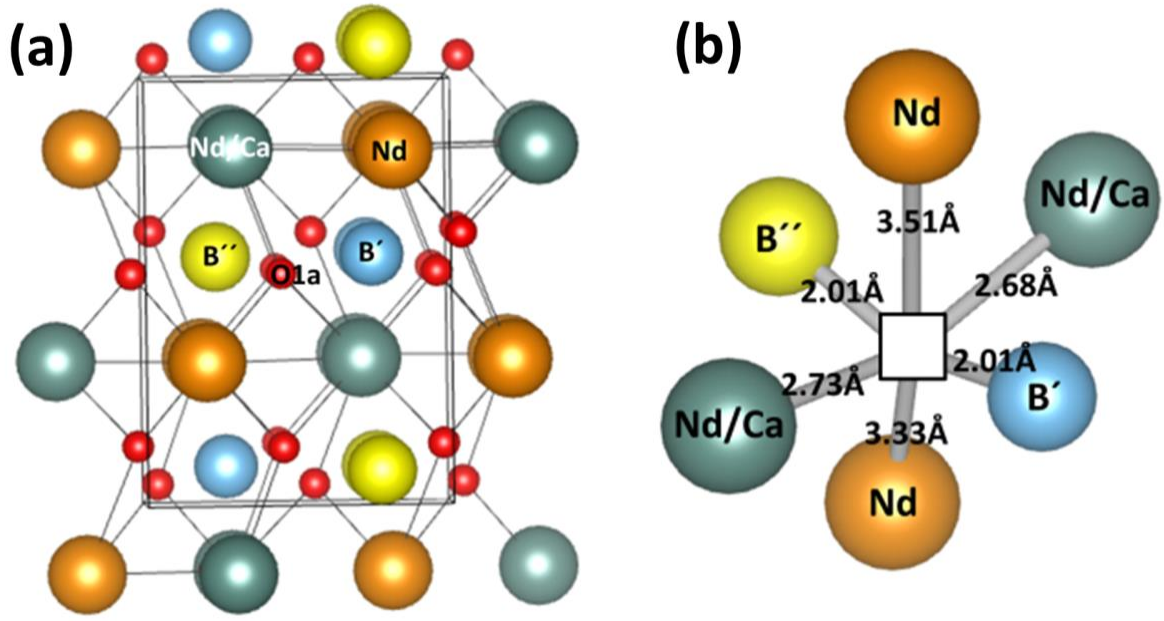

Figure 9. (a) View along the a-axis of the structure of the Ca-containing perovskite $Nd_{1.90}Ca_{0.10}MgTiO_{6-\delta}$; the O1a sites, where oxygen vacancies are located, arrange as rows along the projection axis. (b) Details of the local environment of O1a sites (oxygen vacancies, denoted as □).

$$W = R_W \frac{\tanh\sqrt{j\omega T_W}}{\sqrt{j\omega T_W}} \qquad (2)$$

where R_w is the Warburg resistance and T_w is the Warburg time constant. This latter is related with the effective chemical diffusion coefficient D and effective diffusion thickness L_E by Eq(3):

$$D = L_E^2/T_W \qquad (3)$$

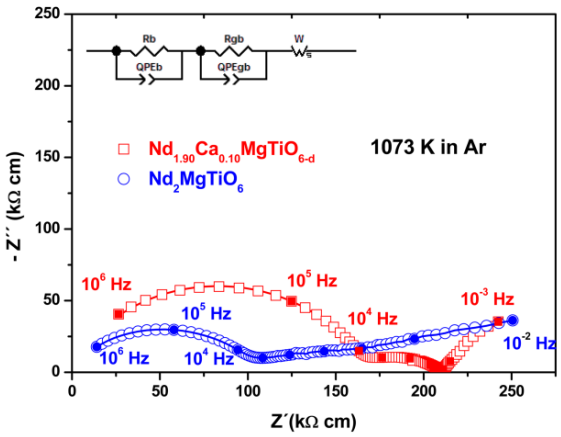

Figure 10. Experimental (symbols) and calculated (solid lines) IS spectra at 1073 K for parent and Ca-containing perovskites recorded in Ar. The inset shows the equivalent circuit use to fit the data.

It is possible to estimate the oxygen diffusion coefficients for the title compounds using a crudely estimated value of L_E of ca 1000 nm; a value similar to those determined in other oxide conductors.[31]

Using the refined values of T_w at 1073 K of 310 s and 450 s for the parent and doped perovskites, values of D can then be determined to 3.3 10^{-13} and 2.2 10^{-13} cm^2s^{-1}, respectively. These values are several orders of magnitude lower than those shown by typical oxide conductors at the same temperature, which are in the range of 10^{-9} to 3 10^{-5} cm^2s^{-1}.[31-35] Thus, the use of the title compounds as electrolyte materials can be discarded due to their low conductivity.

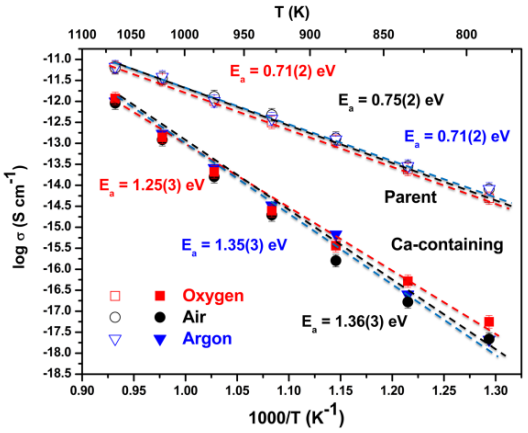

Figure 11. Arrhenius plots of bulk conductivity of parent (open symbols) and Ca-containing (solid symbols) compound in different atmospheres.

On the other hand, ionic conductivity (see Fig. 11) is lower in the substituted compound and the activation energy for conduction higher. High activation energy for ionic conduction may be due to two main reasons:

a) strong interactions of the mobile ions inside the structure limiting the ability to jump to empty positions

b) high correlation of mobile ions hindering net displacements; the ions jump from their positions, but the probability of an effective displacement is limited since most of the adjacent sites are occupied by other ions.

In the present case the structural studies strongly suggest that the main reason for the high activation energies in this perovskite with acceptor dopant is the association of defects $V_O^{\bullet\bullet}$-$Ca_{Nd}^{'}$, previously discussed.

It is possible to estimate the degree of correlation between ions by plotting the real part of conductivity vs frequency at a given temperature. At high frequencies and/or low temperatures, isothermal conductivity data curves show a Jonscher-type[36] power-law dependence given by Eq(4):

$$\sigma'(\omega) \alpha \omega^n \qquad (4)$$

Increasing temperature and/or decreasing frequency leads to a regime of frequency-independent conductivity, which value, σ_{dc}, is the bulk dc conductivity. The power-law frequency dependence given by Eq(4) is related to the existence of cooperative effects in the dynamics of hopping ions; with the fractional exponent n ($0 \le n < 1$) associated with the degree of ion-ion interactions of the ionic hopping process. If no interactions among mobile ions exist, (independent random ion hopping), the exponent n would be 0, whereas n would tend to 1 for a completely correlated motion.[37, 38]

Fig. 12 shows the frequency dependence of the real part of the electrical conductivity at different temperatures for the parent and Ca-substituted compounds.

Although some values of n are slightly higher than unity, that is the upper value with physical meaning,[36] it seems that oxide motion in these perovskites is a strongly correlated process. This can be explained in the parent compound as due to the low concentration of oxygen vacancies, originated by intrinsic defects, which limits the probability for an oxide ion to jump to an empty site since most of the anionic positions are occupied. In the Ca-substituted perovskite the amount of vacancies is higher; however, the interactions between differently charged defects may induce clustering that promotes correlations among oxygen vacancies.

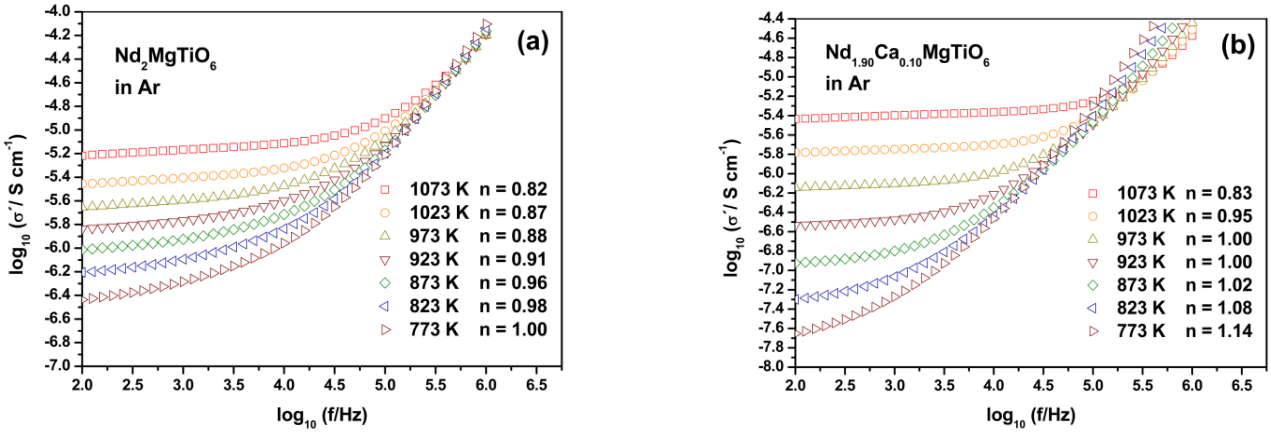

Figure 12. Frequency dependence of the real part of the electrical conductivity at different temperatures of parent (a) and Ca-containing (b) compound in argon atmosphere.

Conclusions

Acceptor doping of Nd_2MgTiO_6 by substitution of up to 5% of Nd^{+3} by Ca^{+2} produces single-phase samples with a noticeable amount of oxygen vacancies. The parent and Ca-containing oxides, display a monoclinic distorted perovskite-like structure with octahedral tilting scheme ($a^-a^-b^+$) and rock-salt like ordering of B-ions. Interestingly, in $Nd_{1.90}Ca_{0.10}MgTiO_{5.94}$ the A-cations are ordered in a rock-salt arrangement as well; this compound being the first case of a type of perovskite predicted by theoretical methods, with the two metal substructures ordered in a rock-salt like manner with Pn symmetry.

Besides this unprecedented arrangement of A- and B-ions, one finds in the acceptor doped oxide an association of defects ($V_O^{\bullet\bullet}$-$Ca_{Nd}^{'}$) which results in the trapping of the created oxygen vacancies. These trapped vacancies display a limited mobility; as a consequence, the oxygen conductivity of the substituted material is lower and its activation energy for oxygen motion is higher than those of the parent oxide, where the concentration of anions vacancies is only due to intrinsic defects. In the two materials, oxygen motion is a strongly correlated process: in the parent one because of the very limited amount of anions vacancies and in the doped oxide due to defect clustering.

Conflicts of interest

There are no conflicts to declare.

Acknowledgements

We thank Agencia Estatal de Investigación (AEI) / Fondo Europeo de Desarrollo Regional (FEDER/UE) for funding the project MAT2016-78362-C4-1-R, and ILL for financial support and for beam time allocation, experiment code 5-31-2462, doi:105291/ILL-DATA.5-22-720. The authors also thank Comunidad de Madrid and European Structural Funds for their financial support to the MATERYENER3-CM (S2013/MIT-2753) project. Financial support from Universidad CEU San Pablo is also acknowledged. We thank Dr. J. Romero de Paz for the magnetic measurements.

References

1. N. Mahato, A. Banerjee, A. Gupta, S. Omar and K. Balani, *Progress in Materials Science*, 2015, **72**, 141-337.
2. H. Hayashi, H. Inaba, M. Matsuyama, N. G. Lan, M. Dokiya and H. Tagawa, *Solid State Ionics*, 1999, **122**, 1-15.
3. T. Ishihara, H. Matsuda and Y. Takita, *Journal of the American Chemical Society*, 1994, **116**, 3801-3803.
4. R. H. Mitchell, *Perovskite: Modern and Ancient*, Ontario (Canada), 2002.
5. J. C. Perez Flores, C. Ritter, D. Perez-Coll, G. C. Mather, F. Garcia-Alvarado and U. Amador, *Journal of Materials Chemistry*, 2011, **21**, 13195-13204.
6. M. Yuste, Perez-Flores, J.C., Romero de Paz, J., Azcondo,M.T., Garcıa-Alvarado, F., Amador, U., *Dalton Trans.*, 2011, **40**, 7908.
7. A. Gomez-Perez, M. T. Azcondo, M. Yuste, J. C. Perez-Flores, N. Bonanos, F. Porcher, A. Munoz-Noval, M. Hoelzel, F. Garcia-Alvarado and U. Amador, *Journal of Materials Chemistry A*, 2016, **4**, 3386-3397.
8. J. C. Pérez-Flores, Pérez-Coll, D., García-Martín, S., Ritter, C., Mather, G.C., Canales-Vázquez, J., Gálvez-Sánchez, M., García-Alvarado, F., Amador, U., *Chemistry of Materials*, 2013, **25**, 2484-2494.
9. S. P. Jiang, *Journal of Materials Science*, 2008, **43**, 6799-6833.
10. W. A. Groen, F. P. F. van Berkel and D. J. W. IJdo, *Acta Crystallographica Section C*, 1986, **42**, 1472-1475.
11. J. Rodríguez-Carvajal, *Physica B: Condensed Matter*, 1993, **192**, 55-69.
12. J. Johnson, *ZView: A software Program for IES Analy*, 2005, **Scribner Associates, Inc.**
13. Z. Maupoey, Azcondo, M.T., Amador, U., Kuhn, A., Perez-Flores, J.C. , Romero de Paz, J., Bonanos, N. , Garcia-Alvarado, F. , *Journal of Materials Chemistry* 2012, **22**, 18033.
14. C. J. Howard, P. W. Barnes, B. J. Kennedy and P. M. Woodward, *Acta Crystallographica Section B*, 2005, **61**, 258-262.
15. J. H. Yang, W. K. Choo, J. H. Lee and C. H. Lee, *Acta Crystallographica Section B*, 1999, **55**, 348-354.
16. Z. Maupoey, M. T. Azcondo, J. C. Perez-Flores, C. Ritter, K. Boulahya, U. Amador and F. Garcia-Alvarado, *Dalton Transactions*, 2014, **43**, 14099-14108.
17. A. Glazer, *Acta Crystallographica Section B*, 1972, **28**, 3384-3392.
18. C. J. Howard, Stokes, H. T.,, *Acta Crystallographica Section B*, 1998, **54**, 782-789.
19. C. J. Howard and H. T. Stokes, *Acta Crystallographica Section A*, 2005, **61**, 93-111.
20. G. King and P. M. Woodward, *Journal of Materials Chemistry*, 2010, **20**, 5785-5796.
21. M. C. Knapp and P. M. Woodward, *Journal of Solid State Chemistry*, 2006, **179**, 1076-1085.
22. P. Woodward, *Acta Crystallographica Section B*, 1997, **53**, 44-66.
23. P. Woodward, *Acta Crystallographica Section B*, 1997, **53**, 32-43.
24. A. Gomez-Perez, Perez-Flores, J.C., Ritter, C., Boulahya, K., Castro, G.R., F. Garcia-Alvarado, G.R., Amador, U., *J. Appl. Cryst.*, 2014, **47**, 745-754.
25. R. Shannon, *Acta Crystallographica Section A*, 1976, **32**, 751-767.
26. B. N. Figgis, Hitchman, M.A., *Ligand Field Theory and Its Applications*, Wiley-VCH, New York, 2000.
27. A. H. Morrish, *The Physical Principles of Magnetism*, R.E. Krieger Publishing Company, Florida, USA, 1983.
28. I. B. Bersuker, *J. Phys.: Conf. Ser.* , 2017, **833**, 012001.
29. V. Polinger, *Journal of Physics Conference Series*, 2013, **428**, 012026.
30. J. T. S. Irvine, D. C. Sinclair and A. R. West, *Advanced Materials*, 1990, **2**, 132-138.
31. P. Jasinski, V. Petrovsky, T. Suzuki and H. U. Anderson, *Journal of the Electrochemical Society*, 2005, **152**, J27-J32.
32. H. Inaba and H. Tagawa, *Solid State Ionics*, 1996, **83**, 1-16.
33. J. L. Routbort, R. Doshi and M. Krumpelt, *Solid State Ionics*, 1996, **90**, 21-27.
34. J. A. Lane, S. J. Benson, D. Waller and J. A. Kilner, *Solid State Ionics*, 1999, **121**, 201-208.
35. R. J. Packer and S. J. Skinner, *Adv. Mater.*, 2010, **22**, 1613-1616.
36. A. K. Jonscher, *Journal of Non-Crystalline Solids*, 1972, **8-10**, 293-315.
37. K. Funke, *Journal of Non-Crystalline Solids*, 1994, **172-174**, 1215-1221.
38. K. L. Ngai and K. Y. Tsang, *Physical Review E*, 1999, **60**, 4511-4517.